

# Four-Dimensional Imaging of ZnO-Coated Alumina Aerogels by Scanning Transmission X-ray Microscopy and Ptychographic Tomography

Juan Wu,<sup>†,||</sup> Xiaohui Zhu,<sup>†,||</sup> David A. Shapiro,<sup>‡</sup> Jonathan R. I. Lee,<sup>§</sup> Tony Van Buuren,<sup>§</sup> Monika M. Biener,<sup>§</sup> Stuart A. Gammon,<sup>§</sup> Tian T. Li,<sup>§</sup> Theodore F. Baumann,<sup>§</sup> and Adam P. Hitchcock<sup>\*,†</sup>

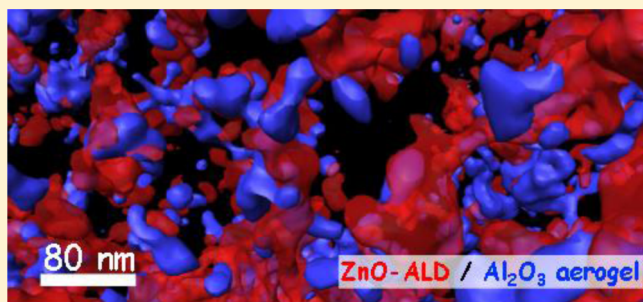
<sup>†</sup>Brockhouse Institute for Materials Research, McMaster University, Hamilton, Ontario L8S 4M1 Canada

<sup>‡</sup>Advanced Light Source, Berkeley Lab, Berkeley, California 94720, United States

<sup>§</sup>Lawrence Livermore National Laboratory, Livermore, California 94550 United States

## Supporting Information

**ABSTRACT:** Functional porous materials are of increasing importance in energy conversion and catalysis. Improved analysis is needed to guide optimization. Four-dimensional (4D) imaging [chemical mapping in three-dimensional (3D) by spectro-tomography] of an Al<sub>2</sub>O<sub>3</sub> aerogel coated with ZnO by atomic layer deposition was performed using soft X-ray ptychography at the Zn L-edge. A two-dimensional spatial resolution of 14(2) nm was achieved. Visualizations of the 3D chemical structure are provided. The degree of ZnO coverage of the surface of the Al<sub>2</sub>O<sub>3</sub> aerogel framework in two different samples was estimated and found to be both thicker and less homogeneous than expected. Other analyses of the 4D results, including the degree of contact between Al<sub>2</sub>O<sub>3</sub> and ZnO, were extracted from the reconstructed 3D data. This pioneering soft X-ray spectro-ptycho-tomography study will anchor further studies of functional porous materials.



## INTRODUCTION

Functional porous materials are attracting increasing attention in the areas of energy conversion and storage, catalysis, and sensing.<sup>1–3</sup> From the viewpoint of materials development for these applications, it is often preferable to introduce the desired functionality by creating a heterostructured system in which a functional species (e.g., catalytic nanoparticle) is deposited on the inner surface of a porous bulk substrate that is prepared by an existing and robust synthetic approach. This strategy can greatly simplify materials optimization in which structural properties of the porous support, such as mechanical stability, thermal stability, and architecture, can be tailored independently from the desired properties of the added functionality. A number of gas-phase and liquid-phase deposition techniques have been developed to uniformly distribute a desired functional material within a porous support material, including atomic layer deposition (ALD),<sup>4–6</sup> wet impregnation,<sup>7</sup> galvanic replacement,<sup>8</sup> and electrodeposition.<sup>9</sup> Previous work has demonstrated the utility of ALD on porous substrates to create functional heterostructured materials with applications ranging from catalysis<sup>4,10</sup> and energy storage<sup>5</sup> to laser-induced X-ray sources.<sup>6</sup> Three-dimensional (3D) characterization of the nanoscale structure and chemistry within these materials is of critical importance because it enables the

following: (i) evaluation of synthetic pathways designed to generate heterostructures with targeted architectures and compositions and (ii) correlation between their structure and performance, which, in turn, can inform the rational design of materials with enhanced properties and behavior.

Four-dimensional (4D) imaging, in this case, quantitative chemical mapping in 3D, is a powerful approach<sup>11</sup> for material characterization, which is often key to fully understand the physical and chemical properties of heterostructured systems. Recently, there have been significant advances in 4D imaging. Electron tomography in transmission electron microscopy (TEM) can be used to acquire the 3D structure of samples.<sup>12</sup> Tilt series tomography has been combined with energy dispersive X-ray spectroscopy (EDS)<sup>13</sup> and electron energy loss spectroscopy (EELS)<sup>11,12,14–16</sup> to provide 4D characterization. These TEM methods are extremely powerful and provide outstanding spatial resolution.

Synchrotron-based microscopies<sup>17–19</sup> with variable incident photon energy or EDS detection provide 4D imaging capabilities which complement EM methods, with certain

Received: July 31, 2018

Revised: October 15, 2018

Published: October 16, 2018

Table 1. Sample and Measurement Details

CODE	details	sample	run	measure
A	6 cycle ALD	FIB cube	May 2017 CLS a-STXM	STXM spectro-tomography at the Zn and Al edges Zn 2p, Al 1s spectra
B	25 cycle ALD	cast from a water suspension	Nov 2016 ALS 5321	ptychographic Zn 2p spectro-tomography

advantages in terms of accessible sample thickness and ability to measure beam-sensitive samples. Soft X-ray scanning transmission X-ray microscopy (STXM) characterizes electronic and chemical structure by imaging with near-edge X-ray absorption fine structure spectral contrast at better than 30 nm spatial resolution.<sup>17,18</sup> STXM provides more analytical information per unit radiation dose than TEM–EELS<sup>20</sup> or TEM–EDS<sup>21</sup> so it is particularly useful for characterizing radiation sensitive materials.<sup>22</sup> In order to perform 3D and 4D imaging by STXM, several methods have been developed, including laminography,<sup>23</sup> serial sectioning,<sup>24</sup> and tilt-series tomography.<sup>25</sup> Haddad et al. first applied soft X-ray STXM tilt-series tomography on gold patterns.<sup>26</sup> The first 4D soft X-ray STXM imaging (tomography at multiple photon energies) was implemented by Johansson et al., who used STXM spectro-tomography to analyze acrylate polyelectrolyte-filled polystyrene microspheres in water.<sup>27</sup> In recent years, STXM tomography has become a mature technique providing useful information on environmental, biological, biogeochemical, and material science samples in both dry and wet conditions.<sup>24,28</sup> However, one of the limitations of soft X-ray STXM tomography is spatial resolution, typically 30–60 nm, which is much lower than EM tomography. The resolution is largely limited by the quality of zone plate (ZP) focusing optics. Recent advances in ZP fabrication have pushed the record spatial resolution for two-dimensional (2D) imaging of high contrast test objects to sub-10 nm,<sup>29</sup> but further progress in that direction seems to be very slow. For practical studies, 4D soft X-ray STXM imaging only provides 25 nm spatial resolution at best.

Ptychography is a coherent diffraction imaging (CDI) technique,<sup>30</sup> which has achieved spatial resolutions well below 10 nm in the soft X-ray region.<sup>31,32</sup> Ptychographic imaging is not limited by focusing optics, such as the ZP in STXM, and has the potential to achieve diffraction limited resolution<sup>33,34</sup> which is given by the Rayleigh diffraction limit of the X-rays and ZP used, which is  $\lambda/(2 \times \text{NA})$ , where  $\lambda$  is the X-ray wavelength and NA is the numerical aperture.  $\text{NA} = n \times \sin \theta$ , where  $n$  is the diffraction order and  $\theta$  is the convergent angle of the incident X-rays. In ptychography, the sample is illuminated with a spot of coherent X-rays which is raster scanned to generate an array of coherent diffraction patterns from overlapping regions on a sample.<sup>19,35,36</sup> Because of the redundant information from overlapping spots, the robustness and rate of convergence of the iterative reconstruction algorithm is greatly improved relative to other CDI methods. In addition, ptychography can be combined with tomography to produce high-resolution 3D nanostructure characterization. For example, Holler et al. recorded a series of 2D ptychographic images of a porous Ta<sub>2</sub>O<sub>5</sub> film sample at different tilt angles and achieved a 3D spatial resolution of 16 nm using 0.2 nm wavelength X-rays.<sup>37</sup> X-ray ptychography was developed over a decade ago in the hard X-ray regime, where high-sensitivity X-ray cameras are readily available, diffraction is stronger, wavelength is very short, and high penetration depths facilitate ease of implementation. Ptychography in the soft X-ray is still under development. Giewekemeyer et al.<sup>38</sup>

first applied soft X-ray ptychography to image a fossil diatom at 517 eV in the “water window”. Soft X-ray ptychographic tomography using phase contrast at a single wavelength has been reported.<sup>39</sup> The first soft X-ray spectro-ptychography measurement was reported in 2011 by Beckers et al.<sup>40</sup> Recently, multi-energy, soft X-ray spectro-ptychography has been used to characterize magnetotactic bacteria,<sup>32</sup> cement hydrates,<sup>41</sup> nanocatalysts,<sup>42</sup> lithium battery systems,<sup>43</sup> and fuel cell membrane electrode assemblies.<sup>44,45</sup> Yu et al.<sup>46</sup> have recently reported the first detailed, soft X-ray spectro-tomography study in which the 3D chemical structure of Li<sub>x</sub>FePO<sub>4</sub> battery electrode material was measured at the Fe L-edge, as a function of the charge/discharge state.

Here, we report a spectro-ptycho-tomography study of the 4D structure of a model heterostructured material, namely an Al<sub>2</sub>O<sub>3</sub> aerogel coated with nanoscale ZnO via ALD. Ptychographic images of the Al<sub>2</sub>O<sub>3</sub>/ZnO heterostructure were recorded at energies above and below the Zn L-edges and at a series of tilt angles. At each tilt angle, quantitative chemical maps of the ZnO were derived from the difference of these images, whereas quantitative chemical maps of the Al<sub>2</sub>O<sub>3</sub> were derived from the pre-Zn L-edge image by subtracting the ZnO signal. These two tomographic tilt series were then reconstructed and the 3D volume representations were combined into a 4D chemical data set.

Direct comparison of the ptychography results to STXM results on a similar sample shows that ptychography provides a dramatic improvement in spatial resolution. Comparison of the X-ray results to TEM imaging and EDS analysis of the same material showed that, for the ALD conditions used, particle growth rather than conformal film formation occurred. This unexpected result is leading to improved understanding of optimal conditions for ALD of ZnO on Al<sub>2</sub>O<sub>3</sub> aerogels. Finally, as one of the first soft X-ray spectro-ptycho tomography studies, this pioneering study paves the way for applications in other nanomaterial systems.

## EXPERIMENTAL SECTION

**Sample Preparation.** The alumina aerogels used in this study were prepared using a two-step sol–gel process, as previously described.<sup>59</sup> Following supercritical drying, the monolith aerogel parts had a bulk density of  $\sim 40 \text{ kg/m}^3$ . Coating of the alumina aerogels with ZnO was achieved via ALD according to established protocols.<sup>4,6,60</sup> In short, the alumina aerogels were exposed to 6 or 25 ALD cycles composed of diethyl zinc (ZnEt<sub>2</sub>) and H<sub>2</sub>O precursor half-cycles in a warm wall reactor (wall and stage temperature of 110 °C). To facilitate handling, the aerogels were kept in their molds during ALD coating. Long pump (20 s), pulse (500 s at  $\sim 133 \text{ Pa}$ ), and nitrogen purge cycles (500 s) during each ALD half-cycle were used to promote uniform coating throughout the porous material.

Samples for STXM and ptychography were prepared by two different methods. One sample preparation method, used for sample A, was focused ion beam (FIB) milling. A 5 nm carbon layer was deposited on a section of the aerogel for thermal conduction. The sample was then FIB sectioned into a 20  $\mu\text{m}$

$\times 30 \mu\text{m} \times 30 \mu\text{m}$  cube and mounted at the tip of a strip of TEM grid. In the other method, used for sample B, the aerogel sample was crushed using a clean scalpel blade and then dispersed in distilled water to get a low concentration dispersion of aerogel powder. A small drop of the solution was dropped on a formvar-coated TEM grid and air-dried. After drying, a single grid strip with the region of interest was excised by scalpel. In both cases, the grid strips were then glued to a brass pin or to the support piece for ptychography and mechanically attached to the STXM or ptychography rotation system. Table 1 summarizes properties of the two samples for which we report results in this paper. Samples were prepared for TEM measurements by pressing copper grids against fragments of the ZnO-coated  $\text{Al}_2\text{O}_3$  aerogels obtained via crushing with a scalpel blade.

**Methods—STXM.** STXM measurements were carried out using the ambient STXM at beamline 10ID-1 at the Canadian light source (CLS).<sup>62</sup> In STXM, monochromatic X-rays are focused by a ZP onto the sample. Images are generated by raster-scanning the sample while detecting the transmitted X-rays. A sequence of images, covering an energy range of interest (“stacks”),<sup>63</sup> is generated for subsequent analysis using aXis2000.<sup>64</sup> For conventional 2D STXM studies, a stack with 91 images was recorded at the Al K edge from 1546–1631 eV and a stack with 105 images was recorded from 1006–1124 eV to encompass the Zn  $L_{2,3}$ -edges. For conventional STXM tomography measurements, images were collected at each angle for energies below and above absorption edges of Zn (1015 and 1055 eV for the L-edge) and Al (1555 and 1571 eV for the K-edge). In total, images were collected at 18 angles from  $0^\circ$  to  $180^\circ$  with a step size of  $10^\circ$  at each energy of interest. TEM studies were performed using a Titan 80-300 scanning TEM system, which was operated at 300 kV for both the TEM and STEM EDS measurements.

**Methods—Ptychographic Tomography and Reconstruction.** Ptychographic measurements were carried out using Nanosurveyor I<sup>65</sup> at the 5.3.2.1 bending magnet beamline at the Advanced Light Source (ALS). A ZP with an outer zone width of 60 nm was used to illuminate the sample. The sample was raster-scanned through the  $\sim 75$  nm focus spot with a step size of 50 nm ( $\sim 30\%$  overlap, possibly higher than the nominal geometric overlap as there is a lot of power outside of the central beam of a ZP focus). The high-frame-rate CCD detector of Nanosurveyor I was used to record diffraction images with a single point exposure time of 150 ms. Ptychographic images were measured at energies below and above the Zn  $L_3$ -edge, at 1010 and 1026.8 eV, respectively, from  $-65^\circ$  to  $+65^\circ$  with a step size of  $10^\circ$ . The ptychography measurements were only performed at the Zn L-edge because the coherent flux on ALS beamline 5.3.2.1 is low at the Al K edge (1570 eV) energy, and a Si bright field filter, used to allow a single time exposure, was overly transparent at the Al K-edge energy. At each energy point and tilt angle, the camera background signal is measured with the beamline shutter closed, and the background is removed in subsequent data processing.<sup>31,55</sup> Ptychographic images were reconstructed using 500 iterations of the relaxed averaged alternating reflection reconstruction algorithm implemented in the SHARP ptychography code developed by the Center for Applied Mathematics for Energy Research Applications.<sup>66</sup>

**Methods—Fourier Ring Correlation.** Two images, ideally measured independently, are required to perform a Fourier ring correlation (FRC) analysis to evaluate the spatial

resolution of reconstructed ptychography images. In order to perform the FRC analysis, each of the recorded diffraction patterns was split into two sub-datasets in a “checker-board” manner to guarantee that the two subsets have no commonality. Then, two images were reconstructed from these two diffraction image subsets. Finally, the FRC between these two reconstructed images was calculated as described in ref 57.

**Methods—Tomographic Reconstruction.** Alignment of different energy images was usually done using the “Zimba” routine in aXis2000. For the ptychographic tomography measurements, further alignment of energy images to correct for image distortion was performed using an auto affine transformation in ImageJ.<sup>67</sup> The STXM chemical maps at each tilt angle were generated as the difference of the aligned 2-energy OD images. For ptychography, the ZnO map was generated as the difference of ptychographic absorption images below (1015 eV) and in the Zn L edge (1026.8 eV). For the ptychographic data, an  $\text{Al}_2\text{O}_3$  map at each angle was derived from the pre-Zn edge OD image, by subtracting 68% of the ZnO map, to correct for the absorption at 1010 eV by ZnO. Alignment of the angle stacks for different components was done manually in aXis2000.

A compressed sensing (CS) algorithm<sup>68</sup> was used for the tomographic reconstruction. The version used is based on the FISTA code for total variation,<sup>69</sup> which is implemented in the Mantis analysis package (available for free at <http://spectromicroscopy.com/>).<sup>70</sup> CS reconstruction methods are more robust than alternatives such as the simultaneous iterative reconstruction technique, which allowed us to greatly reduce the number of tilt angles measured, while obtaining excellent reconstruction quality.<sup>69</sup> The motivation for developing CS methods for tomography was to reduce the overall radiation dose and thus allow tomography of radiation sensitive materials.<sup>69</sup> Although the metal oxide aerogel system in this study is relatively resistant to radiation damage, it is important to note that the total measurement time was dramatically reduced via the use of CS, which is significant because STXM-tomography and ptycho-tomography are relatively slow methods. Even though only 19 tilt angles were measured, the 4 energy STXM tomography measurement of FIB aerogel sample A took 20 h while the 14 angle, 2-energy ptychography tomography measurement of aerogel sample B took 9 h.

**Methods—Quantitative Colocalization Analysis.** The 3D dataset from the tomographic reconstruction was split into a sequence of depth slices with a thickness of 40 nm for STXM dataset A, and 7.5 nm for the ptychography dataset B. At each  $(x,y)$  position within a depth slice, we sum the number of voxels which are exclusively  $\text{Al}_2\text{O}_3$  (“only  $\text{Al}_2\text{O}_3$ ”), those exclusively ZnO (“only ZnO”), and those which have some signal of  $\text{Al}_2\text{O}_3$  and ZnO (“colocalization”), using threshold values determined automatically from the Otsu method.<sup>56</sup> The relative concentration (RC) at  $(x,y)$  is then defined as the ratio of the number of a certain type of voxel (only  $\text{Al}_2\text{O}_3$ , only ZnO, colocalization) to the sum of all types (only  $\text{Al}_2\text{O}_3$  + only ZnO + colocalization), within that layer. Finally, to generate the curves displayed in Figures 4c and 6b, this process is repeated for each depth slice and the RC values as a function of position of the depth slice are derived along the X-ray propagation direction. The detailed quantitative colocalization analysis was performed using in-house Python code which is provided in the Supporting Information.

## RESULTS

**Spectroscopy of the Aerogel Samples.** Figure 1 presents the Zn  $L_{2,3}$  X-ray absorption spectra (XAS) of ZnO

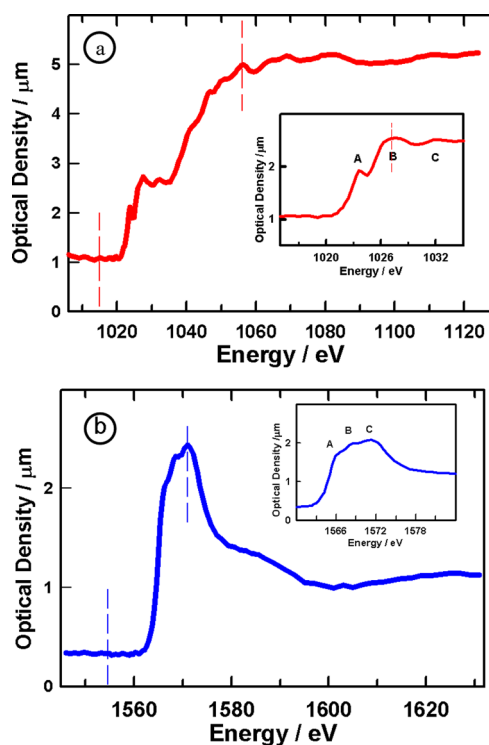


**Figure 1.** XAS of ZnO and  $\text{Al}_2\text{O}_3$  extracted from an identical area of appended and aligned STXM stacks of the ZnO/ $\text{Al}_2\text{O}_3$  aerogel sample A. (a) Zn  $L_{2,3}$  spectrum of pure ZnO derived from the stack spectrum by subtracting the contribution of  $\text{Al}_2\text{O}_3$  and converting the result to OD per nm (OD1). (b) Al K spectrum of pure  $\text{Al}_2\text{O}_3$  derived from the stack spectrum by subtracting the contribution of ZnO and converting the result to OD1. The inset in each panel shows an expanded view of the near edge region. The dashed vertical lines indicate the energies used for 2-energy chemical mapping. Further details are provided in the text and Supporting Information Figure S1.

and Al K XAS of  $\text{Al}_2\text{O}_3$ . These spectra of the pure materials were derived from the average spectrum of a  $3\ \mu\text{m} \times 3\ \mu\text{m}$  area of the ZnO/ $\text{Al}_2\text{O}_3$  aerogel (sample A), prepared by FIB milling. Details of the sample and measurements are given in Table 1. The spectrum of pure ZnO was isolated from the spectrum of the mixed species sample by subtracting a scaled version of the elemental response spectrum (OD1) of  $\text{Al}_2\text{O}_3$  from the Zn  $L_3$  region, whereas the spectrum of pure  $\text{Al}_2\text{O}_3$  was obtained by subtracting a scaled version of the elemental response spectrum (OD1) of ZnO from the Al K-edge region, as presented in Supporting Information Figure S1. Here, OD1 is the optical density (OD) of a chemical species (either the elemental or the actual material) with 1 nm thickness at standard density. The scale factors were chosen so that the difference has a spectral shape that matches (within a constant factor) to the elemental response spectrum of each species in the pre- and post-near edge region—see Figure S1c,d. That factor is then the average thickness of that material in the area measured (Figure S1a). The average spectrum of this region corresponded to a mixture of 80 nm ZnO and 200 nm  $\text{Al}_2\text{O}_3$  at normal densities.

Figure 1 shows the OD1 spectra of pure ZnO and pure  $\text{Al}_2\text{O}_3$ . The inset shows an expansion of the near edge region. In the  $\text{Zn}^{2+}$  ground state, the 3d orbital is fully occupied so the lowest unoccupied Zn levels are 4s, followed by 4p and 4d.<sup>47</sup> Therefore, the lowest energy features of the Zn  $L_3$  XAS correspond to Zn  $2p_{3/2} \rightarrow 4s$  excitations. Peak A is attributed to Zn  $2p_{3/2} \rightarrow 4s$  excitations while peaks B and C are Zn  $2p_{3/2} \rightarrow 4d$  excitations.<sup>48–50</sup> The Al K spectrum of the aerogel is similar to that of the  $\theta$  phase of  $\text{Al}_2\text{O}_3$ .<sup>51</sup> It has three distinct features, shoulder A at 1566 eV, peak B at 1568 eV, and peak C at 1572 eV, which are assigned to excitations associated with the tetrahedral  $\text{AlO}_4$  (A) and octahedral  $\text{AlO}_6$  (B,C) local coordination environments.<sup>51,52</sup> The intensity scales of the Zn L-edge and Al K-edge spectra in Figure 1 are quantitative, expressed in terms of OD per unit thickness. This was established by matching the pre- and post-edge intensities to that predicted for the elemental compositions from standard tabulations<sup>53</sup> and the density of the bulk materials (ZnO  $d = 5.61\ \text{g}/\text{cm}^3$ ;  $\text{Al}_2\text{O}_3$ ,  $d = 3.95\ \text{g}/\text{cm}^3$ )—see Supporting Information Figure S1c,d.

Images at two energies (a stack map) were used to measure the Zn and Al distributions in the ZnO/ $\text{Al}_2\text{O}_3$  aerogel sample. A stack map is the difference between two STXM OD images, one measured at the energy of a characteristic X-ray absorption resonance (“on resonance”) and the other measured below the absorption threshold for the edge of interest (“off resonance”). Figure 2a presents a 2D projection map of the ZnO and derived from the difference between aligned STXM OD images at 1055 and 1015 eV. Figure 2b is the map of  $\text{Al}_2\text{O}_3$  derived from OD images at 1571 and 1555 eV. Supporting

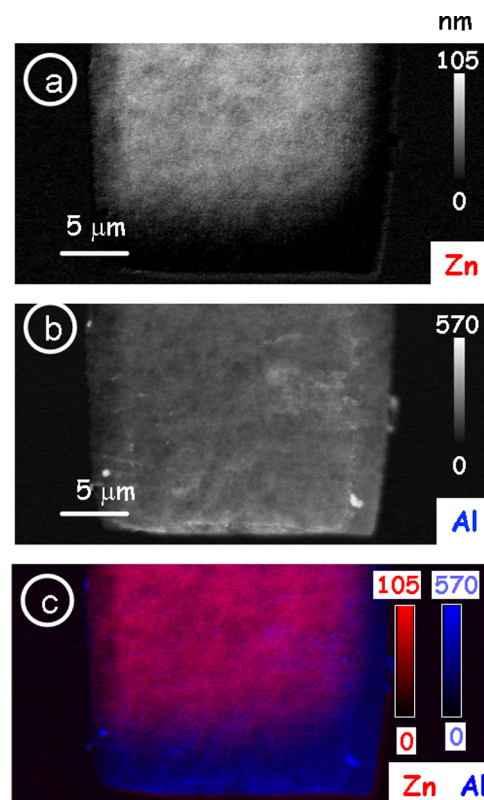


**Figure 2.** STXM 2D chemical maps at  $0^\circ$  tilt angle of a ZnO/ $\text{Al}_2\text{O}_3$  aerogel (sample A). (a)  $\text{Al}_2\text{O}_3$ . (b) ZnO. (c) Color-coded composite map of  $\text{Al}_2\text{O}_3$  (blue), ZnO (red). The gray and color bar scales are thickness in nanometer.

**Information** Figure S2 presents the four STXM OD images used to derive the stack maps in Figure 2a,b. The gray scales in Figure 2a,b indicate the thickness in nm, determined by taking the ratio of the difference in OD at the above and below-edge energies, to that of the difference in the OD1 values at the same two energies (see Figure 1), where OD1 is the OD of ZnO or Al<sub>2</sub>O<sub>3</sub> at standard density and a thickness of 1 nm. Figure 2c is a rescaled color composite of the ZnO (red) and Al<sub>2</sub>O<sub>3</sub> (blue) stack maps in Figure 2a,b, which reveals the spatial correlation of these two elements. If both species were uniformly distributed over the whole of the FIB section, all pixels would be a uniform shade of purple. In fact, the lower part of the section is predominantly blue, indicating that the ion beam has depleted the ZnO during the FIB sample preparation.

**Conventional STXM Spectro-Tomography of ZnO/Al<sub>2</sub>O<sub>3</sub> Aerogel, Sample A.** Figure 3 presents results from 4D

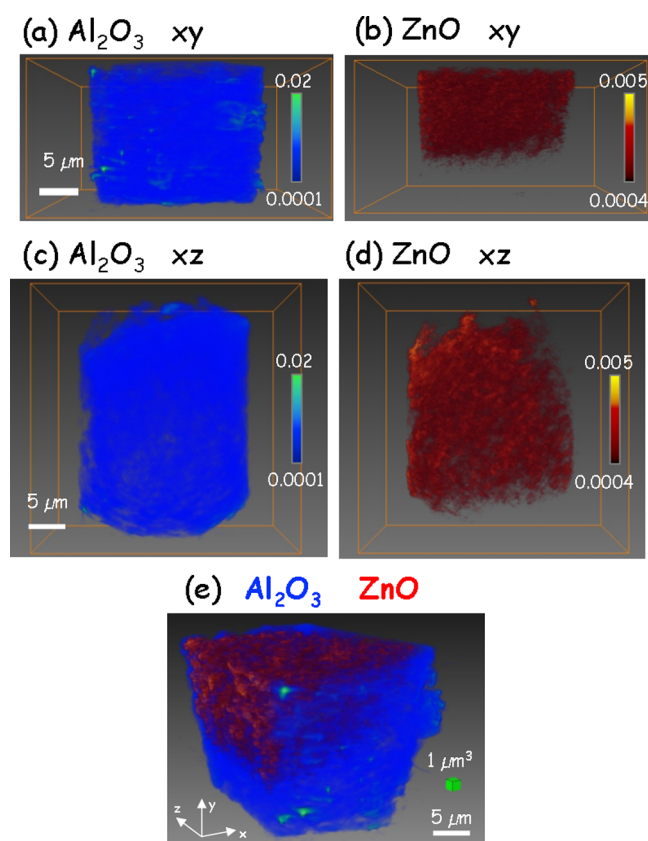


**Figure 3.** 3-dimensional volume rendering of Al<sub>2</sub>O<sub>3</sub> (blue) and ZnO (red) in the ZnO/Al<sub>2</sub>O<sub>3</sub> aerogel FIB sample A, derived from TXM spectro-tomography. (a,b) *xy* views. (c,d) *xz* views. (*z* is direction of X-ray beam). (e) 4D image, a color-coded composite of the two components with Al<sub>2</sub>O<sub>3</sub> in blue and ZnO in red. The segmentation thresholds, determined by the automatic Otsu method,<sup>56</sup> were 0.0004 for ZnO and 0.0001 for Al<sub>2</sub>O<sub>3</sub>.

STXM imaging of the FIB-prepared ZnO/Al<sub>2</sub>O<sub>3</sub> aerogel, sample A, in the form of volume renderings of the Zn and Al 3D maps. The voxel size is 40 nm. The blue color is Al<sub>2</sub>O<sub>3</sub>, and the red color is ZnO. Figure 3a,b are the front view, whereas Figure 3c,d are the top view. When examining the two 3D chemical maps from the front views (Figure 3a,b), one observes that the bottom and right edges of the sample are heavily damaged in terms of depletion of ZnO, which was

caused by the FIB milling. A similar situation is seen in Figure 3c,d, where ZnO depletion damage is evident close to the top and bottom surface. The 4D chemical representation (Figure 3e) clearly shows the spatial correlation of the two chemical maps and the position of the mass loss of ZnO. The relatively large scale of the sample required extensive milling to obtain the desired sample size. The porous structure of the aerogel allowed energetic ions in the FIB process to penetrate into the interior of the structure. As a result, ZnO relatively far from the milling surface was damaged.

Figure 4a shows a surface rendering of the center (5 μm × 5 μm × 5 μm) volume of the FIB sample, a region where there

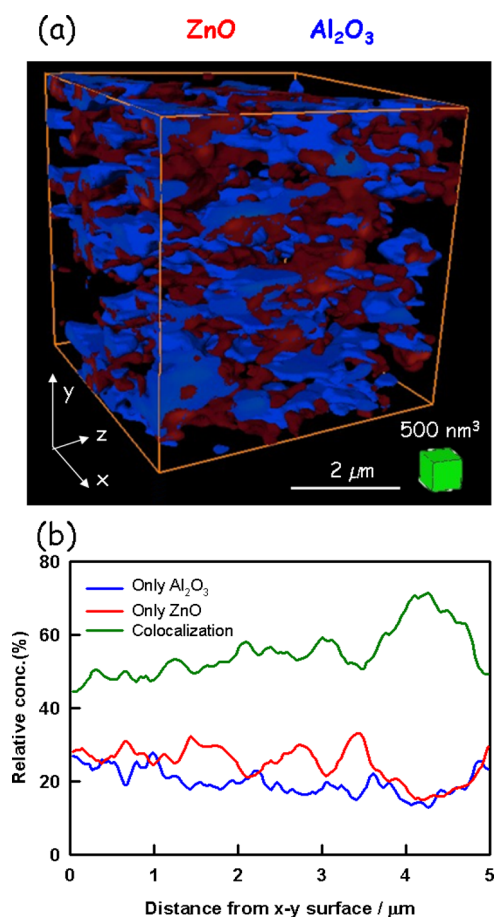


**Figure 4.** (a) Surface rendering of color-coded composite of the ZnO (red) and Al<sub>2</sub>O<sub>3</sub> (blue) 3D distributions from reconstruction of STXM spectro-tomography on ZnO/Al<sub>2</sub>O<sub>3</sub> aerogel (sample A), in a 5 × 5 × 5 μm<sup>3</sup> cube from the center of Figure 3e. The Otsu threshold for ZnO was 0.0004, whereas that for Al<sub>2</sub>O<sub>3</sub> was 0.0001. (b) Relative concentration (RC) curves of ZnO, Al<sub>2</sub>O<sub>3</sub>, and “colocalization”, derived for *xy* slices averaged through the *z* direction.

appears to be negligible ion beam damage. Red in Figure 4a indicates ZnO, selected using an Otsu threshold of 0.0004, whereas blue represents Al<sub>2</sub>O<sub>3</sub> selected using an Otsu threshold of 0.0001. For comparison, the voxel intensity range of the region shown in Figure 4 runs from 0.0000 to 0.0015 for ZnO and 0.0000 to 0.0019 for Al<sub>2</sub>O<sub>3</sub>. In order to quantitatively evaluate the distributions of Al<sub>2</sub>O<sub>3</sub> and ZnO in the composite, the RC<sup>54</sup> of Al<sub>2</sub>O<sub>3</sub> and ZnO in the aerogel was calculated as a function of distance from the sample surface (*xy*). Here, RC is defined as the ratio of the amounts of a certain species (only Al<sub>2</sub>O<sub>3</sub>, only ZnO, or both Al<sub>2</sub>O<sub>3</sub> and

ZnO) relative to the sum of all three species, averaged over a number of voxels. More details can be found in the [Experimental Methods](#) section. [Figure 4b](#) plots the RC of only Al<sub>2</sub>O<sub>3</sub> (blue), only ZnO (red), and both ZnO and Al<sub>2</sub>O<sub>3</sub> (“colocalization”, green) as a function of the distance across the central (5 μm)<sup>3</sup> volume. While the Al<sub>2</sub>O<sub>3</sub> spatial distribution is relatively uniform and unstructured, that of the ZnO shows larger spatial variations in the RC, which suggests that much of the ZnO is present as “de-localized” nanoclusters rather than a conformal thin film. This interpretation is confirmed by complementary TEM and TEM–EDS measurements (see below). Nevertheless, the distribution of the two components generally follows the same trend, indicating a significant uniformity of the aerogel sample prepared via ALD, on the ~30 nm spatial scale of STXM spectro-tomography.

**Spectro-Ptychography and Spectro-Ptycho-Tomography of ZnO/Al<sub>2</sub>O<sub>3</sub> Aerogel, Sample B.** [Figure 5a,b](#) shows

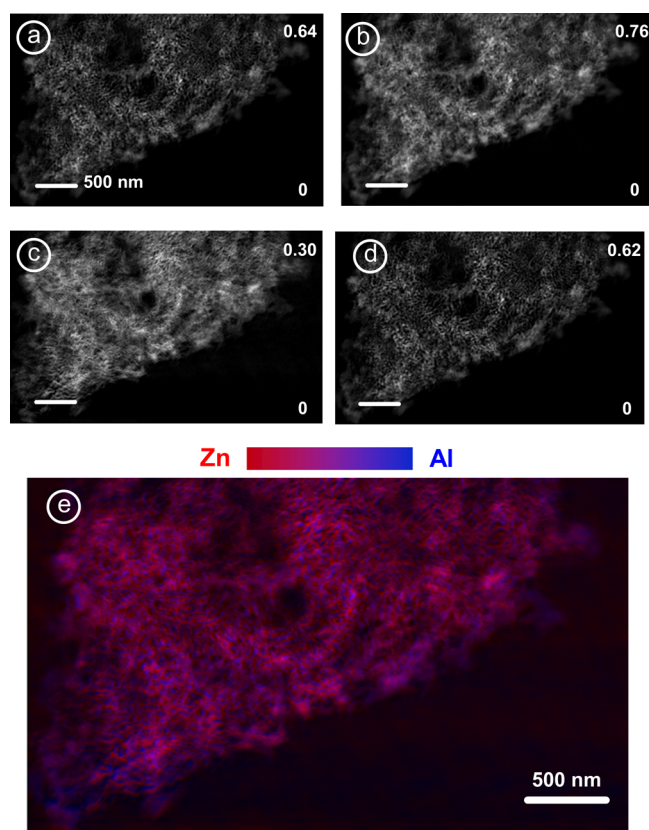


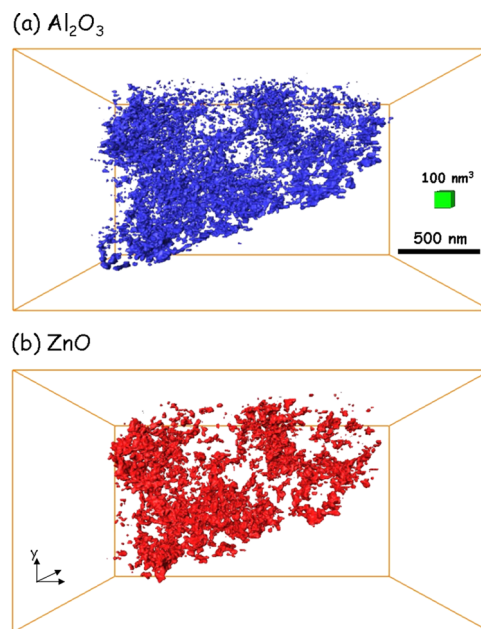
**Figure 5.** Ptychography absorption images of ZnO/Al<sub>2</sub>O<sub>3</sub> aerogel (sample B) at (a) 1010 eV and (b) 1026.8 eV. (c) ZnO chemical map ( $OD_{1026.8\text{eV}} - OD_{1010\text{eV}}$ ). (d) Derived Al<sub>2</sub>O<sub>3</sub> chemical map (see text). (e) Color composite of the two component maps, ZnO in red, Al<sub>2</sub>O<sub>3</sub> in blue.

the ptychography 2D absorption images of the ZnO/Al<sub>2</sub>O<sub>3</sub> aerogel, sample B, at 1010 and 1026.8 eV, which correspond to the pre-edge and Zn L<sub>3</sub> absorption resonance energy of ZnO (see [Figure 1a](#)). The ptychography absorption image is generated from  $-\ln(A_{\text{py}}/I_0)$ , where  $A_{\text{py}}$  is the amplitude of the reconstruction of a 2D ptychographic image and  $I_0$  is the incident photon intensity. [Figure 5c](#) is the ZnO distribution in the ZnO/Al<sub>2</sub>O<sub>3</sub> sample, derived from the difference between the ptychography absorption images in [Figure 5a,b](#). The Al<sub>2</sub>O<sub>3</sub>

distribution was extracted from the pre-edge signal at 1010 eV by subtracting the ZnO signal at 1010 eV which is  $0.68 \times [OD(1026.8) - OD(1010)]$ , where the factor 0.68 is the ratio  $OD(1010)/[OD(1026.8) - OD(1010)]$  for ZnO (see [Figure 1](#)). This estimate of the Al<sub>2</sub>O<sub>3</sub> signal is presented in [Figure 5d](#). [Figure 5e](#) is a scaled color composite of the ZnO (red) and estimated Al<sub>2</sub>O<sub>3</sub> (blue) signals in the ZnO/Al<sub>2</sub>O<sub>3</sub> aerogel sample. The purple colored pixels correspond to columns where there is both ZnO and Al<sub>2</sub>O<sub>3</sub>. The existence of relatively pure red and blue areas, in addition to purple, indicates that there is a non-uniform coating of ZnO. However, 3D maps of the two chemical components are needed to determine if the ZnO and Al<sub>2</sub>O<sub>3</sub> are in contact, or are spatially separated and only accidentally at the same point of the 2D image.

[Supporting Information](#) [Figure S3a,c](#) shows the projections at  $-5^\circ$  tilt angle of the reconstructed 3D images of ZnO and Al<sub>2</sub>O<sub>3</sub>, respectively. These regenerated 2D chemical images can be directly compared to the 2D projection chemical maps of ZnO and Al<sub>2</sub>O<sub>3</sub> at about the same tilt angle, displayed in [Figure 5c,d](#). The differences between the 2D chemical maps and the projections at the same tilt angle from the 3D reconstruction are presented as [Figure S3b,d](#) and histograms of the difference OD maps are presented as [Figure S3e,f](#). This difference analysis indicates that there is a good match between the reconstruction and the 2D projection images, which is better for Al<sub>2</sub>O<sub>3</sub>. For ZnO, the deviation may be related to spatial distortion of the sample in the ptychography images, caused by the high dose used.

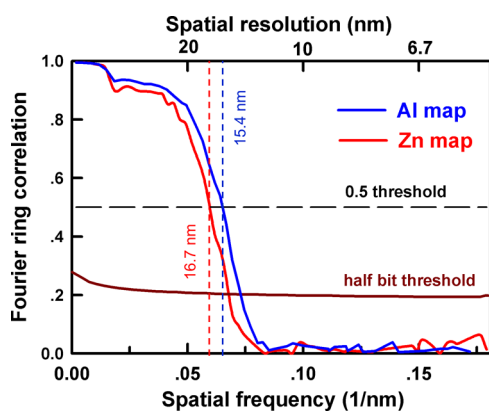
[Figure 6](#) shows surface renderings of the CS reconstruction of the 3D distributions of Al<sub>2</sub>O<sub>3</sub> and ZnO derived from the spectro-ptycho-tomography measurement of the irregular water cast sample B. Thresholds of 0.0018 (Al) and 0.0026 (Zn), derived using the Otsu auto threshold procedure,<sup>56</sup> were



**Figure 6.** 3D surface rendering of ZnO and Al<sub>2</sub>O<sub>3</sub> from ptychography of ZnO/Al<sub>2</sub>O<sub>3</sub> aerogel (sample B). View at  $0^\circ$  of (a) Al<sub>2</sub>O<sub>3</sub> (blue), derived from the signal at 1010 eV minus 68% of the ZnO signal. (b) ZnO (red) ( $OD_{1026.8\text{eV}} - OD_{1010\text{eV}}$ ). The voxel size is  $(5.6 \times 5.6 \times 5.6)$  nm<sup>3</sup>. The Otsu thresholds used were 0.0018 for the Al<sub>2</sub>O<sub>3</sub> signal and 0.0026 for the ZnO signal.

used to derive these distributions. For comparison, the voxel intensity ranges of the region shown in Figure 4 runs from 0 to 0.0103 for Al<sub>2</sub>O<sub>3</sub> and 0 to 0.011 for ZnO. With the higher spatial resolution provided by spectro-ptycho-tomography, the Al<sub>2</sub>O<sub>3</sub> and ZnO spatial distributions are more clearly defined than with STXM tomography (Figure 4). The overall morphology is generally very similar, indicating that the ZnO is attached to the Al<sub>2</sub>O<sub>3</sub> aerogel framework. However, the ZnO distribution is clearly “clumpier”, suggesting less uniform distributions and a non-uniform ZnO ALD coating of the Al<sub>2</sub>O<sub>3</sub> framework.

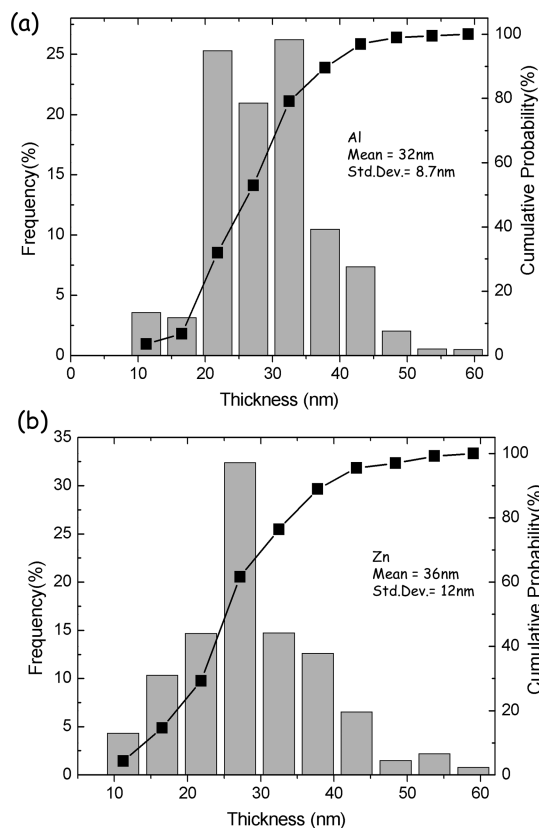
To evaluate the spatial resolution of the 2D ptychography stack maps (Figure 5c,d), the FRC method<sup>57</sup> was used with results displayed in Figure 7. For the ZnO ptychographic stack



**Figure 7.** Spatial resolution estimated from FRC of the ZnO and Al<sub>2</sub>O<sub>3</sub> ptychography maps (Figure 5c,d) (sample B).

map (Figure 5c), the FRC analysis (red, Figure 7) indicates a spatial resolution of 16.7 nm, using the 0.5 threshold (dashed black line, Figure 7a), or 14.6 nm if the conventional half-bit threshold (dark red line, Figure 7a) is used. For the Al<sub>2</sub>O<sub>3</sub> ptychographic stack map (Figure 5d), the FRC analysis (blue, Figure 7) indicates a spatial resolution of 15.4 nm (0.5 threshold) or 13.7 nm (1/2-bit threshold). In other evaluations of the spatial resolution of ptychography using Nanosurveyor I on beamline 5.3.2.1, the resolution is typically higher on resonance than off-resonance, whereas the opposite is the case for this data. The similarity of the estimated resolution evaluated from off- and on-resonance images suggests that this type of aerogel sample is a special case because it has a nanostructure which diffracts strongly at all photon energies so it is really ideal for ptychographic imaging. Compared with the ZnO and Al<sub>2</sub>O<sub>3</sub> stack maps measured with conventional STXM (Figure 2a,b for 2D, and Figure 4a for 3D), it is clear that the spatial resolution of the ptychography maps and 3D spectro-ptycho-tomography 4D imaging is significantly higher than that of the corresponding STXM results.

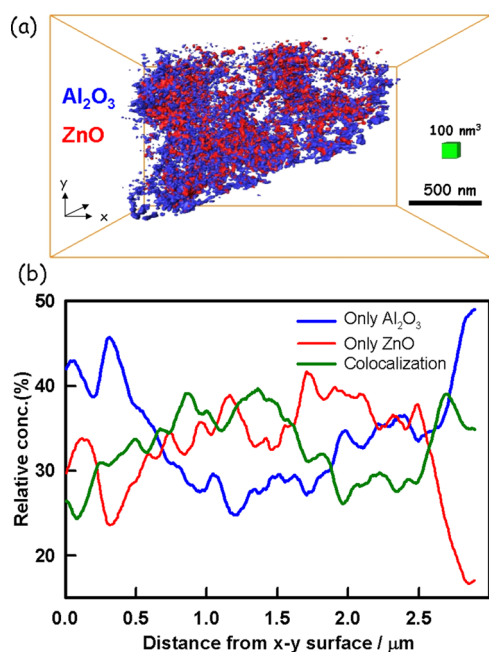
In order to further evaluate the structural properties of the Al<sub>2</sub>O<sub>3</sub>/ZnO composite, the distributions of the size of the Al<sub>2</sub>O<sub>3</sub> and ZnO components were quantified from the tomography results using the open source “Bone J” plugin in ImageJ software.<sup>58</sup> This software first measures the distance of each solid voxel to the nearest empty voxel. It then measures the radius of the largest sphere containing that voxel which does not include empty voxels. It then removes all redundant spheres. The diameter of the sphere with the largest radius is considered as the size of the particle containing that voxel. Figure 8a,b presents histograms of the distributions of sizes of



**Figure 8.** Histograms of the size distribution of (a) Al<sub>2</sub>O<sub>3</sub> and (b) ZnO, in the aerogel sample measured by ptychography (sample B), derived using the “Bone J” plugin in Image J. The square data points and associated curve are the cumulative probability of the size distributions.

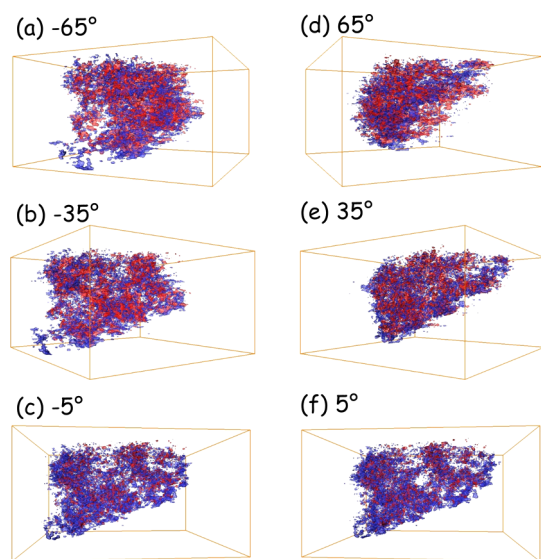
the Al<sub>2</sub>O<sub>3</sub> and ZnO components, with a lower value cutoff of 10 nm. The black squares and curve in Figure 8 correspond to the cumulative probability of the sizes of Al<sub>2</sub>O<sub>3</sub> and ZnO. This analysis shows that the size of the Al<sub>2</sub>O<sub>3</sub> and ZnO components ranges from 10 to 60 nm with a size below 40 nm at a cumulative probability of 95%. The average size of the Al<sub>2</sub>O<sub>3</sub> regions is 32 ± 9 nm while that of the ZnO particles is 36 ± 12 nm, where the variation band is taken from the histograms in Figure 8.

Figure 9a presents a surface rendering of the ptychographic 4D reconstruction of the Al<sub>2</sub>O<sub>3</sub>/ZnO composite with Al<sub>2</sub>O<sub>3</sub> in blue and ZnO in red, derived using Otsu thresholds of 0.0018 for the Al<sub>2</sub>O<sub>3</sub> signal and 0.0026 for the ZnO signal. In order to investigate the detailed distribution of Al<sub>2</sub>O<sub>3</sub> and ZnO in the aerogel, the RCs of Al<sub>2</sub>O<sub>3</sub> and ZnO in the aerogel were calculated as a function of distance from the sample surface (xy). Similarly to Figure 4b, the RC<sup>54</sup> is defined as the ratio of the amounts of a certain species (only Al<sub>2</sub>O<sub>3</sub>, only ZnO or both Al<sub>2</sub>O<sub>3</sub> and ZnO) relative to that of the sum of all three species, averaged over a set of voxels. Figure 9b plots the RC of only Al<sub>2</sub>O<sub>3</sub> (blue), only ZnO (red), and both ZnO and Al<sub>2</sub>O<sub>3</sub> (“colocalization”, green), as a function of distance from the surface. In this volume, there is more Al<sub>2</sub>O<sub>3</sub> toward the surface and less Al<sub>2</sub>O<sub>3</sub> in the middle region (50–250 nm from the surface of the 1.5<sup>3</sup> μm<sup>3</sup> volume), where the Al<sub>2</sub>O<sub>3</sub> is distributed more uniformly. The distribution of ZnO is almost opposite to that of Al<sub>2</sub>O<sub>3</sub>, with more ZnO in the middle region and less ZnO toward the surface. The “colocalization” volume (green in Figure 9b), where both Al<sub>2</sub>O<sub>3</sub> and ZnO components are



**Figure 9.** (a) Surface-rendered color-coded composite of the 3D distributions of ZnO (red) and Al<sub>2</sub>O<sub>3</sub> (blue) from spectro-ptychotomography of ZnO/Al<sub>2</sub>O<sub>3</sub> aerogel (sample B). The Otsu thresholds used were 0.0018 for the Al<sub>2</sub>O<sub>3</sub> signal and 0.0026 for the ZnO signal. (b) Relative concentration (RC) curves of the two pure components and their co-localized amounts in *xy* slices, averaged through the *z* direction.

present, has a distribution similar to that of ZnO. It is clear that the ZnO does not fully cover the Al<sub>2</sub>O<sub>3</sub> phase, as ~30% of the Al<sub>2</sub>O<sub>3</sub> (blue) is not coated by ZnO. More surface-rendered views of the 4D maps at different tilt angles are shown in Figure 10. These views show that the aerogel piece deposited from the water suspension has an irregular shape. To estimate the porosity of the sample, a 1.5 μm<sup>3</sup> cube in the center of the sample has been extracted, as shown in Figure S4. The threshold values were the same as in Figure 9. Images of ~20



**Figure 10.** Views at six different tilted angles of the reconstruction of the ptychotomography data for sample B. (a) -65°, (b) -35°, (c) -5°, (d) 5°, (e) 35°, and (f) 65°.

nm thick *xy* planes at different depths along the *z* direction are presented in Figure S4b. The volume fractions of the two components in the *xy* planes along the *z* direction are plotted in Figure S4c. The porosity of the cube is 89(2)%, which is reduced from the porosity of the uncoated Al<sub>2</sub>O<sub>3</sub>,<sup>59</sup> as expected. The volume fraction of ZnO is 5.6(1.2)%, and the Al<sub>2</sub>O<sub>3</sub> is 6.3(1.4)%. The uncertainties were estimated by subdividing the data into four regions, evaluating each parameter within the subvolumes, and then taking the standard deviation. Note that there are larger systematic uncertainties associated with the segmentation threshold.

A movie of the 4D ptychography result (color-coded composite of the ZnO and Al<sub>2</sub>O<sub>3</sub> reconstructions) is presented in the Supporting Information. It shows the 3D chemical structure of the composite imaged from a number of angles and with detailed interior views. Supporting Information Figure S5 is one frame from the movie. It clearly shows the presence of non-conformal ZnO coatings (red) on the Al<sub>2</sub>O<sub>3</sub> aerogel framework (blue). Three 500 nm<sup>3</sup> cubes are enlarged in Figure S6 to show samples of the spatial distributions of the two components in several areas of the water-cast sample B. The 3D spatial resolution has been evaluated from intensity line profiles, as shown in Figure S7. Using a 10–90% intensity metric, and measuring profiles at three locations in each of the *xy* and *yz* planes, the spatial resolution is estimated to be 18 nm (3 pixels) for the *xy* plane and 24 nm (4 pixels) for the *yz* plane.

**TEM of the ZnO/Al<sub>2</sub>O<sub>3</sub> Aerogel.** Figure 11a,b are high-resolution TEM (HR-TEM) images of the ZnO-coated Al<sub>2</sub>O<sub>3</sub> aerogel. Needle- and leaflike motifs of the aerogel framework are readily observed in Figure 11a. These are consistent with the structures reported for Al<sub>2</sub>O<sub>3</sub> aerogels prepared via the synthetic pathway used to make the samples of this study.<sup>59</sup> The surfaces of the Al<sub>2</sub>O<sub>3</sub> aerogel are decorated by nanoparticles with dimensions ranging from a few nanometers to more than 30 nm. Z-contrast imaging (Figure 11c) reveals that these nanoparticles contain a higher-Z element than the aerogel scaffold, which strongly indicates that they arise from the ZnO ALD coating. This assignment is further supported by energy dispersive spectroscopy (EDS) measurements (data not shown) that indicate the presence of only Al, O, and Zn in the sample (Cu from the TEM sample grid was also observed). The EDS data also reveal that the RC of each of these elements varies as a function of position within the sample. Significantly, the ZnO nanoparticles are highly crystalline and typically observed to be single crystals, as demonstrated by Figure 11b. Attempts to obtain the atomic resolution of the Al<sub>2</sub>O<sub>3</sub> network were unsuccessful as the sample fragments reacted to the incident electron beam by moving on the Cu grid, which is attributed to charging of the Al<sub>2</sub>O<sub>3</sub>. We were surprised initially by the apparently significant differences between the TEM and ptychography images. There are three contributions to these differences. First, all the 2D X-ray images are integrating through a substantial thickness of the aerogel sample, whereas a much thinner region of the sample was imaged by TEM. Second, because of the lower spatial resolution of ptychography than TEM, the fine spatial features of the sample are blurred. Supporting Information Figure S8 compares a smoothed version of the TEM image smoothed to 15 nm with the ZnO ptychography 2D projection image (Figure S4a) to explore this aspect. Third, some radiation damage to the very fragile Al<sub>2</sub>O<sub>3</sub> aerogel framework likely occurred in the conditions used for the TEM image in Figure 11c.

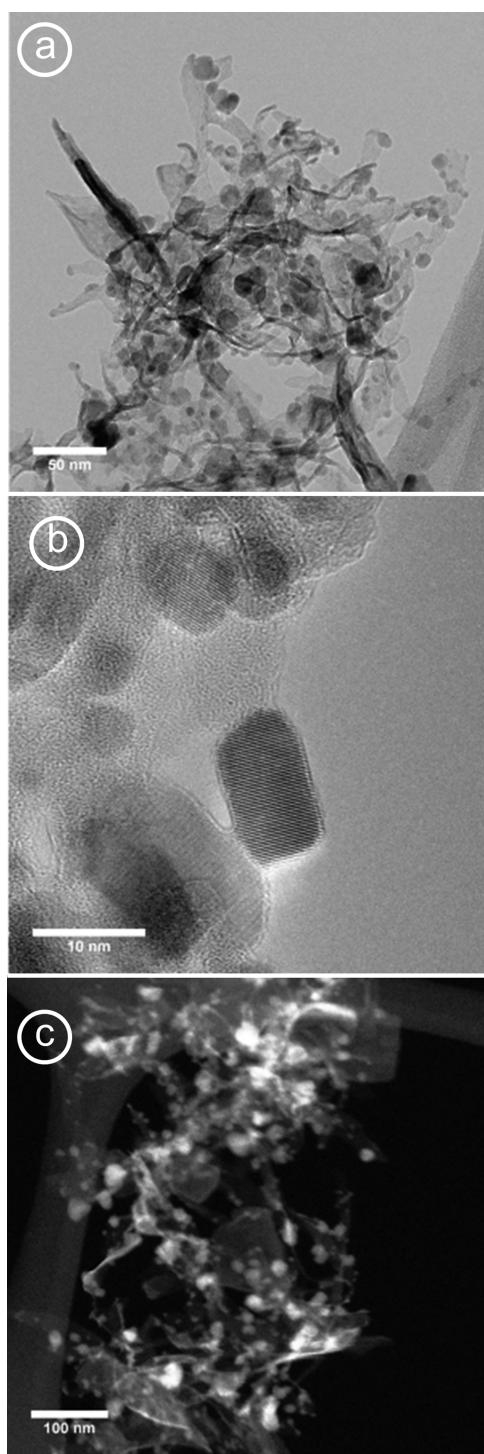


**Figure 11.** (a) Transmission electron micrograph of an  $\text{Al}_2\text{O}_3$  aerogel coated with 25 ALD cycles of ZnO. Three morphologies are indicated:  $\sim 10\text{--}30$  nm strongly scattering, square/spherical clusters of single crystals (ZnO). Elongated, strongly scattering rods (ZnO), weakly scattering sheetlike material (alumina). (b) High-resolution TEM showing crystal planes of ZnO. (c) Z-contrast scanning transmission electron micrograph of the same material in which the higher-Z ZnO coating appears white and the  $\text{Al}_2\text{O}_3$  appears gray.

## DISCUSSION

The  $\text{Al}_2\text{O}_3/\text{ZnO}$  heterostructures provide an excellent system for demonstrating the utility of spectro-ptycho-tomography for 4D characterization of functional nanostructured materials for

several reasons: (i) the samples are prepared via established and robust synthetic procedures that enable control over the final architecture, composition, and properties, including manipulation of electronic structure. (ii) They offer significant structural complexity—hierarchical pore structures with nanoscale surface coatings. (iii) Both ZnO and  $\text{Al}_2\text{O}_3$  have catalytic applications. (iv) Spectroscopic-based speciation, rather than density-based segmentation, is used. The comparative STXM spectro-tomography at both the Zn L-edge and the complementary Al K-edge points to further advantages of multiedge spectro-ptycho-tomography.

As observed in other soft X-ray STXM/ptychography comparisons,<sup>30,31</sup> ptychography provides significantly improved spatial resolution relative to STXM in both 2D and 3D. Although the ptychography measurements were made only at the Zn L-edges due to technical reasons, this was sufficient to determine images and quantitative maps of both the ZnO and  $\text{Al}_2\text{O}_3$  components. From detailed analyses of the 3D distributions, it was possible to estimate the degree to which the ALD deposited ZnO covered the  $\text{Al}_2\text{O}_3$  aerogel framework. In the ptychography measurement of sample B, the ZnO coverage of the  $\text{Al}_2\text{O}_3$  aerogel was estimated to be 33(5)%. A similar co-localization analysis of the STXM spectro-tomography reconstruction gave a derived ZnO coverage of 55(8)% (uncertainties from standard deviation of results from subdividing the data). This slightly larger value is likely due to the lower spatial resolution of STXM than ptychography, although the different sample preparations could also play a role.

The ability to derive the surface coverage of the ALD coating, combined with the structural and spectroscopic information available for the aerogel scaffold and ALD layer using spectro-ptycho-tomography, provided significant new insights about ZnO ALD on porous  $\text{Al}_2\text{O}_3$  frameworks. It has been reported that the mode of ZnO ALD growth on bulk  $\text{Al}_2\text{O}_3$  (specifically sapphire) is dependent on the sample temperature during deposition. Island growth is encountered at  $150^\circ\text{C}$  on a planar substrate, while layer-by-layer growth occurs at  $220^\circ\text{C}$ .<sup>60</sup> The measurements performed in this study conclusively demonstrate that island (/nanoparticle) formation occurs on the  $\text{Al}_2\text{O}_3$  even with only 6 ALD cycles at a sample temperature of  $110^\circ\text{C}$ , suggesting that the lower-temperature growth mode extends from planar surfaces to the curved framework of the  $\text{Al}_2\text{O}_3$  aerogel. Furthermore, the dimensions of the ZnO nanocrystals (tens of nm) dramatically exceeded the sizes that were expected from the reported deposition rates during the initial stages of ALD ( $\sim 0.2$  nm/cycle, for an expected conformal film with a thickness  $\leq 5$  nm). This behavior is consistent with a growth mechanism in which adsorbates migrate across the substrate surface to form larger nanoparticles, thereby minimizing interfacial and surface energies.

Comparison with the TEM data for the  $\text{Al}_2\text{O}_3/\text{ZnO}$  material further illustrates the value of spectro-ptycho-tomography as a complementary or alternative method for high-resolution materials characterization. There is clearly strong qualitative and quantitative agreement between the structures derived from the two techniques. Such close correlation confirms that the formation of ZnO nanocrystals is not an artifact of irradiation with the electron beam, that is, via beam damage/heating, and thus greater weight can be placed on the TEM data. Without the complementary spectro-ptycho-tomography measurements, beam damage could have remained a concern if

one was attempting to distinguish between layer-by-layer and island growth using only TEM, particularly given that the sample reacted by moving under the electron beam during HR-TEM measurements of the  $\text{Al}_2\text{O}_3$  scaffold. This movement of the sample has an additional significance in which it precluded high spatial resolution diffraction or spectroscopy studies to identify the phase and bonding of the aerogel using TEM. The X-ray-based methods were able to address this gap in knowledge via assignment of the  $\theta$  phase of  $\text{Al}_2\text{O}_3$  and identification of both tetrahedral ( $\text{AlO}_4$ ) and octahedral ( $\text{AlO}_6$ )-bonding environments of Al within the aerogel. The combination of techniques also indicates that the structure of the  $\text{Al}_2\text{O}_3$  aerogel remains unchanged through the formation of the ZnO layer, which demonstrates the robustness of the aerogel as a scaffold for functionalization by ALD.

Spectro-ptycho-tomography has far broader applicability than this study of ZnO ALD on an  $\text{Al}_2\text{O}_3$  aerogel. The enhanced spatial resolution of spectro-ptycho-tomography versus conventional STXM spectro-tomography, combined with the localized structural and chemical information derived from the technique, has the potential for significant impact on development of improved nanoscale and nanostructured functional materials. This study demonstrates that 4D spectro-ptycho-tomography can provide quantitative information regarding the size, distribution, and electronic structure (and, by extension, local bonding and phase) of nanoscale coatings, the exposed surface area of both template and coating, the amount of interface between them, and the pore architecture. Such information is of direct value in understanding relationships between the structure and properties/performance of nanostructured systems including catalysts, for example, for identifying active sites, the efficiency of specific architectures, mass transport through the material, degradation pathways, and so forth. Furthermore, assignment of the material structure and bonding can be used in a feedback loop to improve synthetic pathways for generating designer materials. Significantly, spectro-ptycho-tomography does not impose as stringent limits over sample thickness and radiation sensitivity as does comparable electron beam techniques, making it a powerful complementary or alternative 4D analysis method.

With the development of near diffraction-limited synchrotron radiation (DLSR) facilities such as Max IV in Sweden and Sirius in Brazil as well as DLSR upgrade activities and plans at many third generation facilities, it is clear that the types of dramatic improvements in 4d imaging presented in this work will become routinely available in the near future.<sup>61</sup> The recently commissioned COSMIC beamline at the ALS, which is dedicated to ptychography, will be an outstanding facility to continue this type of 4D imaging.

## CONCLUSIONS

STXM spectro-tomography and ptychography spectro-tomography were performed on several different  $\text{Al}_2\text{O}_3$  aerogel samples, and 4D images were generated by reconstruction. The spatial resolution calculated by FRC shows that the 2D and 3D spatial resolution in the ptychography results was significantly improved relative to corresponding conventional STXM measurements. A quantitative analysis of both the STXM and ptychography tomography results gave detailed information about the ALD coatings. Non-uniform coating of ZnO by ALD was documented by both STXM and ptychography 4D imaging. The quantitative and qualitative structural informa-

tion provided by the X-ray methods has a direct value for evaluating and optimizing the ZnO ALD process and illustrate their broad applicability for characterizing heterostructures on nanometer length scales.

## ASSOCIATED CONTENT

### Supporting Information

The Supporting Information is available free of charge on the ACS Publications website at DOI: 10.1021/acs.jpcc.8b07363.

Derivation of quantitative spectra of pure ZnO and pure  $\text{Al}_2\text{O}_3$ ; STXM OD images of ZnO/ $\text{Al}_2\text{O}_3$ ; precision, surface rendering, frame of the video, and expanded views of ptycho-tomography reconstruction; line profiles through slices of ptycho-tomography volumes, comparison of smoothed TEM and ptychography images, flow diagram of co-localization analysis, and the python code used to generate for the colocalization analysis results (PDF)

4D chemical mapping of sample B recorded by spectro-ptycho-tomography (MPG)

## AUTHOR INFORMATION

### Corresponding Author

\*E-mail: [aph@mcmaster.ca](mailto:aph@mcmaster.ca). Phone: 905 525-9140 ext. 24749.

### ORCID

Adam P. Hitchcock: 0000-0002-1598-7886

### Author Contributions

<sup>†</sup>J.W. and X.Z. contributed equally to this work.

### Notes

The authors declare no competing financial interest.

The data that support the findings of this study are available from the corresponding author (A.P.H.) on request.

## ACKNOWLEDGMENTS

Research is supported by NSERC (Canada). We thank Travis Casagrande for excellent FIB operation. Ptychography performed at ALS beamline 5.3.2.1, ALS is supported by the Department of Energy, Basic Energy Sciences under contract no. DE-AC02-05CH11231. The ptychography data analysis software is supported by the Center for Applied Mathematics for Energy Research Applications (CAMERA), which is a partnership between Basic Energy Sciences (BES) and Advanced Scientific Computing Research (ASRC) at the US Department of Energy. STXM tomography was performed at beamline 10ID1 at the CLS which is supported by the Canada Foundation for Innovation, Natural Sciences and Engineering Research Council of Canada, the University of Saskatchewan, the Government of Saskatchewan, Western Economic Diversification Canada, the National Research Council Canada, and the Canadian Institutes of Health Research. We thank Jian Wang for his excellent support of the CLS-SM facility. Portions of this work were performed under the auspices of the U.S. Department of Energy (DoE), Office of Basic Energy Sciences, Division of Materials Science and Engineering by Lawrence Livermore National Laboratory under contract no. DE-AC52-07NA27344.

## REFERENCES

- (1) Biener, J.; Stadermann, M.; Suss, M.; Worsley, M. A.; Biener, M. M.; Rose, K. A.; Baumann, T. F. Advanced Carbon Aerogels for Energy Applications. *Energy Environ. Sci.* **2011**, *4*, 656.

- (2) Bagge-Hansen, M.; Wichmann, A.; Wittstock, A.; Lee, J. R. I.; Ye, J.; Willey, T. M.; Kuntz, J. D.; van Buuren, T.; Biener, J.; Bäumer, M.; et al. Quantitative Phase Composition of TiO<sub>2</sub>-Coated Nanoporous Au Monoliths by X-ray Absorption Spectroscopy and Correlations to Catalytic Behavior. *J. Phys. Chem. C* **2014**, *118*, 4078–4084.
- (3) Qiu, S.; Zhao, F.; Zenasni, O.; Li, J.; Shih, W.-C. Nanoporous Gold Disks Functionalized with Stabilized G-Quadruplex Moieties for Sensing Small Molecules. *ACS Appl. Mater. Interfaces* **2016**, *8*, 29968–29976.
- (4) Biener, M. M.; Biener, J.; Wichmann, A.; Wittstock, A.; Baumann, T. F.; Bäumer, M.; Hamza, A. V. ALD Functionalized Nanoporous Gold: Thermal Stability, Mechanical Properties, and Catalytic Activity. *Nano Lett.* **2011**, *11*, 3085–3090.
- (5) Ye, J.; Baumgaertel, A. C.; Wang, Y. M.; Biener, J.; Biener, M. M. Structural Optimization of 3D Porous Electrodes for High-Rate Performance Lithium Ion Batteries. *ACS Nano* **2015**, *9*, 2194–2202.
- (6) Biener, M. M.; Biener, J.; Wang, Y. M.; Shin, S. J.; Tran, I. C.; Willey, T. M.; Pérez, F. N.; Poco, J. F.; Gammon, S. A.; Fournier, K. B.; et al. Atomic Layer Deposition-Derived Ultra-Low-Density Composite Bulk Materials with Deterministic Density and Composition. *ACS Appl. Mater. Interfaces* **2013**, *5*, 13129–13134.
- (7) Ge, X.; Chen, L.; Zhang, L.; Wen, Y.; Hirata, A.; Chen, M. Nanoporous Metal Enhanced Catalytic Activities of Amorphous Molybdenum Sulfide for High-Efficiency Hydrogen Production. *Adv. Mater.* **2014**, *26*, 3100–3104.
- (8) Zhao, Z. L.; Wang, Q.; Zhang, L. Y.; An, H. M.; Li, Z.; Li, C. M. Galvanic Exchange-Formed Ultra-Low Pt Loading on Synthesized Unique Porous Ag-Pd Nanotubes for Increased Active Sites toward Oxygen Reduction Reaction. *Electrochim. Acta* **2018**, *263*, 209–216.
- (9) Yang, S.; Deng, B.; Ge, R.; Zhang, L.; Wang, H.; Zhang, Z.; Zhu, W.; Wang, G. Electrodeposition of Porous Graphene Networks on Nickel Foams as Supercapacitor Electrodes with High Capacitance and Remarkable Cyclic Stability. *Nanoscale Res. Lett.* **2014**, *9*, 672.
- (10) King, J. S.; Wittstock, A.; Biener, J.; Kucheyev, S. O.; Wang, Y. M.; Baumann, T. F.; Giri, S. K.; Hamza, A. V.; Baeumer, M.; Bent, S. F. Ultralow Loading Pt Nanocatalysts Prepared by Atomic Layer Deposition on Carbon Aerogels. *Nano Lett.* **2008**, *8*, 2405–2409.
- (11) Torruella, P.; Arenal, R.; de la Peña, F.; Saggi, Z.; Yedra, L.; Eljarrat, A.; López-Conesa, L.; Estrader, M.; López-Ortega, A.; Salazar-Alvarez, G.; Nogués, J.; Ducati, C.; Midgley, P. A.; Peiró, F.; Estradé, S. 3D Visualization of the Iron Oxidation State in FeO/Fe<sub>3</sub>O<sub>4</sub> Core-Shell Nanocubes from Electron Energy Loss Tomography. *Nano Lett.* **2016**, *16*, 5068–5073.
- (12) Goris, B.; Turner, S.; Bals, S.; Van Tendeloo, G. Three-Dimensional Valency Mapping in Ceria Nanocrystals. *ACS Nano* **2014**, *8*, 10878–10884.
- (13) Slater, T. J. A.; Janssen, A.; Camargo, P. H. C.; Burke, M. G.; Zaluzec, N. J.; Haigh, S. J. STEM-EDX Tomography of Bimetallic Nanoparticles: A Methodological Investigation. *Ultramicroscopy* **2016**, *162*, 61–73.
- (14) Jarausch, K.; Thomas, P.; Leonard, D. N.; Twisten, R.; Booth, C. R. Four-Dimensional STEM-EELS: Enabling Nano-Scale Chemical Tomography. *Ultramicroscopy* **2009**, *109*, 326–337.
- (15) Hörl, A.; Trügler, A.; Hohenester, U. Tomography of Particle Plasmon Fields from Electron Energy Loss Spectroscopy. *Phys. Rev. Lett.* **2013**, *111*, 076801.
- (16) Wang, X.; Langelier, B.; Shah, F. A.; Korinek, A.; Bugnet, M.; Hitchcock, A. P.; Palmquist, A.; Grandfield, K. Biomineralization at Titanium Revealed by Correlative 4D Tomographic and Spectroscopic Methods. *Adv. Mater. Interfaces* **2018**, *5*, 1800262.
- (17) Hitchcock, A. P. Soft X-Ray Imaging and Spectromicroscopy. *Handbook of Nanoscopy*; Van Tendeloo, G., Van Dyck, D., Pennycook, J. S., Eds.; Wiley, 2012; Vol. II, pp 745–792.
- (18) Hitchcock, A. P. Soft X-ray spectromicroscopy and ptychography. *J. Electron Spectrosc. Relat. Phenom.* **2015**, *200*, 49–63.
- (19) Thibault, P.; Guizar-Sicairos, M.; Menzel, A. Coherent Imaging at the Diffraction Limit. *J. Synchrotron Radiat.* **2014**, *21*, 1011–1018.
- (20) Wang, J.; Botton, G. A.; West, M. M.; Hitchcock, A. P. Quantitative Evaluation of Radiation Damage to Polyethylene Terephthalate by Soft X-Rays and High-Energy Electrons. *J. Phys. Chem. B* **2009**, *113*, 1869–1876.
- (21) de A Melo, L. G.; Hitchcock, A. P.; Berejnov, V.; Susac, D.; Stumper, J.; Botton, G. A. Evaluating Focused Ion Beam and Ultramicrotome Sample Preparation for Analytical Microscopies of the Cathode Layer of a Polymer Electrolyte Membrane Fuel Cell. *J. Power Sources* **2016**, *312*, 23–35.
- (22) Zhu, X.; Hitchcock, A. P.; Bittencourt, C.; Umek, P.; Krüger, P. Individual Titanate Nanoribbons Studied by 3D-Resolved Polarization Dependent X-Ray Absorption Spectra Measured with Scanning Transmission X-Ray Microscopy. *J. Phys. Chem. C* **2015**, *119*, 24192–24200.
- (23) Xu, F.; Helfen, L.; Suhonen, H.; Elgrabli, D.; Bayat, S.; Reischig, P.; Baumbach, T.; Cloetens, P. Correlative Nanoscale 3D Imaging of Structure and Composition in Extended Objects. *PLoS One* **2012**, *7*, e50124.
- (24) Hitchcock, A. P.; Araki, T.; Ikeura-Sekiguchi, H.; Iwata, N.; Tani, K. 3d chemical mapping of toners by serial section scanning transmission X-ray microscopy. *J. Phys. IV* **2003**, *104*, 509–512.
- (25) Schmid, G.; Zeitvogel, F.; Hao, L.; Ingino, P.; Kuerner, W.; Dynes, J. J.; Karunakaran, C.; Wang, J.; Lu, Y.; Ayers, T.; et al. Synchrotron-based Chemical Nano-Tomography of Microbial Cell-Mineral Aggregates in Their Natural, Hydrated State. *Microsc. Microanal.* **2014**, *20*, 531–536.
- (26) Haddad, W. S.; McNulty, I.; Trebes, J. E.; Anderson, E. H.; Levesque, R. A.; Yang, L. Ultrahigh-Resolution X-Ray Tomography. *Science* **1994**, *266*, 1213–1215.
- (27) Johansson, G. A.; Tyliczszak, T.; Mitchell, G. E.; Keefe, M. H.; Hitchcock, A. P. Three-Dimensional Chemical Mapping by Scanning Transmission X-Ray Spectromicroscopy. *J. Synchrotron Radiat.* **2007**, *14*, 395–402.
- (28) Schmid, G.; Obst, M.; Wu, J.; Hitchcock, A. P. 3D Chemical Imaging of Nanoscale Biological, Environmental, and Synthetic Materials by Soft X-Ray STXM Spectrotomography. *X-ray and Neutron Techniques for Nanomaterials Characterization*; Kumar, C. S. S. R., Eds.; Springer-Verlag: Berlin Heidelberg, 2016; pp 43–94.
- (29) Chao, W.; Fischer, P.; Tyliczszak, T.; Reka, S.; Anderson, E.; Naulleau, P. Real Space Soft X-Ray Imaging at 10 Nm Spatial Resolution. *Opt. Express* **2012**, *20*, 9777.
- (30) Miao, J.; Sandberg, R. L.; Song, C. Coherent X-Ray Diffraction Imaging. *IEEE J. Sel. Top. Quantum Electron.* **2012**, *18*, 399–410.
- (31) Shapiro, D. A.; Yu, Y.-S.; Tyliczszak, T.; Cabana, J.; Celestre, R.; Chao, W.; Kaznatcheev, K.; Kilcoyne, A. L. D.; Maia, F.; Marchesini, S.; et al. Chemical Composition Mapping with Nanometre Resolution by Soft X-Ray Microscopy. *Nat. Photonics* **2014**, *8*, 765–769.
- (32) Zhu, X.; Hitchcock, A. P.; Bazylnski, D. A.; Denes, P.; Joseph, J.; Lins, U.; Marchesini, S.; Shiu, H.-W.; Tyliczszak, T.; Shapiro, D. A. Measuring Spectroscopy and Magnetism of Extracted and Intracellular Magnetosomes Using Soft X-Ray Ptychography. *Proc. Natl. Acad. Sci. U.S.A.* **2016**, *113*, E8219–E8227.
- (33) Miao, J.; Ishikawa, T.; Robinson, I. K.; Murnane, M. M. Beyond Crystallography: Diffractive Imaging Using Coherent X-Ray Light Sources. *Science* **2015**, *348*, 530–535.
- (34) Edo, T. B.; Batey, D. J.; Maiden, A. M.; Rau, C.; Wagner, U.; Pešić, Z. D.; Waigh, T. A.; Rodenburg, J. M. Sampling in X-Ray Ptychography. *Phys. Rev. A: At, Mol, Opt. Phys.* **2013**, *87*, 053850.
- (35) Rodenburg, J. M.; Hurst, A. C.; Cullis, A. G.; Dobson, B. R.; Pfeiffer, F.; Bunk, O.; David, C.; Jefimovs, K.; Johnson, I. Hard-X-Ray Lensless Imaging of Extended Objects. *Phys. Rev. Lett.* **2007**, *98*, 034801.
- (36) Thibault, P.; Dierolf, M.; Bunk, O.; Menzel, A.; Pfeiffer, F. Probe Retrieval in Ptychographic Coherent Diffractive Imaging. *Ultramicroscopy* **2009**, *109*, 338–343.
- (37) Holler, M.; Diaz, A.; Guizar-Sicairos, M.; Karvinen, P.; Färm, E.; Härkönen, E.; Ritala, M.; Menzel, A.; Raabe, J.; Bunk, O. X-Ray Ptychographic Computed Tomography at 16 Nm Isotropic 3D Resolution. *Sci. Rep.* **2014**, *4*, 3857.

- (38) Giewekemeyer, K.; Thibault, P.; Kalbfleisch, S.; Beerlink, A.; Kewish, C. M.; Dierolf, M.; Pfeiffer, F.; Salditt, T. Quantitative Biological Imaging by Ptychographic X-Ray Diffraction Microscopy. *Proc. Natl. Acad. Sci. U.S.A.* **2010**, *107*, 529–534.
- (39) Venkatakrisnan, S. V.; Farmand, M.; Yu, Y.-S.; Majidi, H.; van Benthem, K.; Marchesini, S.; Shapiro, D. A.; Hexemer, A. Robust X-Ray Phase Ptycho-Tomography. *IEEE Signal Process. Lett.* **2016**, *23*, 944–948.
- (40) Beckers, M.; Senkbeil, T.; Gorniak, T.; Reese, M.; Giewekemeyer, K.; Gleber, S.-C.; Salditt, T.; Rosenhahn, A. Chemical Contrast in Soft X-Ray Ptychography. *Phys. Rev. Lett.* **2011**, *107*, 208101.
- (41) Bae, S.; Taylor, R.; Shapiro, D.; Denes, P.; Joseph, J.; Celestre, R.; Marchesini, S.; Padmore, H.; Tyliczszak, T.; Warwick, T.; et al. Soft X-ray Ptychographic Imaging and Morphological Quantification of Calcium Silicate Hydrates (C-S-H). *J. Am. Ceram. Soc.* **2015**, *98*, 4090–4095.
- (42) Wise, A. M.; Weker, J. N.; Kalirai, S.; Farmand, M.; Shapiro, D. A.; Meirer, F.; Weckhuysen, B. M. Nanoscale Chemical Imaging of an Individual Catalyst Particle with Soft X-Ray Ptychography. *ACS Catal.* **2016**, *6*, 2178–2181.
- (43) Yu, Y.-S.; Kim, C.; Shapiro, D. A.; Farmand, M.; Qian, D.; Tyliczszak, T.; Kilcoyne, A. L. D.; Celestre, R.; Marchesini, S.; Joseph, J.; et al. Dependence on Crystal Size of the Nanoscale Chemical Phase Distribution and Fracture in  $\text{Li}_x\text{FePO}_4$ . *Nano Lett.* **2015**, *15*, 4282–4288.
- (44) Hitchcock, A. P.; Wu, J.; Lee, V.; Appathurai, N.; Tyliczszak, T.; Shiu, H.-W.; Shapiro, D. A.; Berejnov, V.; Susac, D.; Stumper, J. Progress in Soft X-Ray Microscopy Characterization of PEM Fuel Cell Catalyst Layers. *Microsc. Microanal.* **2016**, *22*, 1290–1291.
- (45) Putz, A. M. V.; Susac, D.; Berejnov, V.; Wu, J.; Hitchcock, A. P.; Stumper, J. (Plenary) Doing More with Less: Challenges for Catalyst Layer Design. *ECS Trans.* **2016**, *75*, 3–23.
- (46) Yu, Y.-S.; Farmand, M.; Kim, C.; Liu, Y.; Grey, C. P.; Stobridge, F. C.; Tyliczszak, T.; Celestre, R.; Denes, P.; Joseph, J.; et al. Three Dimensional Localization of Nanoscale Battery Reactions Using Soft X-Ray Tomography. *Nat. Commun.* **2018**, *9*, 921.
- (47) Chen, C.-Y.; Lai, K.-Y.; Lo, J.-W.; Lin, C.-A.; Chiu, S.-H.; Chao, Y.-C.; He, J.-H. Electronic Structures of Well-Aligned Er-Doped ZnO Nanorod Arrays. *J. Nanosci. Nanotechnol.* **2011**, *11*, 10615–10619.
- (48) Yuste, M.; Escobar Galindo, R.; Caretti, I.; Torres, R.; Sánchez, O. Influence of the oxygen partial pressure and post-deposition annealing on the structure and optical properties of ZnO films grown by dc magnetron sputtering at room temperature. *J. Phys. D Appl. Phys.* **2012**, *45*, 025303.
- (49) Wang, M.; Ren, F.; Zhou, J.; Cai, G.; Cai, L.; Hu, Y. N Doping to ZnO Nanorods for Photoelectrochemical Water Splitting under Visible Light: Engineered Impurity Distribution and Terraced Band Structure. *Sci. Rep.* **2015**, *5*, 12925.
- (50) Cho, D.-Y.; Kim, J. H.; Na, K. D.; Song, J.; Hwang, C. S.; Park, B.-G.; Kim, J.-Y.; Min, C.-H.; Oh, S.-J. Spectroscopic Evidence for Limited Carrier Hopping Interaction in Amorphous ZnO Thin Film Spectroscopic Evidence for Limited Carrier Hopping Interaction in Amorphous ZnO Thin Film. *Appl. Phys. Lett.* **2014**, *26*, 261903.
- (51) Kato, Y.; Shimizu, K.-i.; Matsushita, N.; Yoshida, T.; Yoshida, H.; Satsuma, A.; Hattori, T. Quantification of aluminium coordinations in alumina and silica-alumina by Al K-edge XANES. *Chem. Phys.* **2001**, *3*, 1925–1929.
- (52) Cabaret, D.; Sainctavit, P.; Ildefonse, P.; Flank, A.-M. Full Multiple-Scattering Calculations on Silicates and Oxides at the Al K Edge. *J. Phys.: Condens. Matter* **1996**, *8*, 3691–3704.
- (53) Henke, B. L.; Gullikson, E. M.; Davis, J. C. X-Ray Interactions: Photoabsorption, Scattering, Transmission, and Reflection at  $E = 50$ –30,000 eV,  $Z = 1$ –92. *Atomic Data Nucl. Data Tables* **1993**, *54*, 181–342.
- (54) Yang, F.; Liu, Y.; Martha, S. K.; Wu, Z.; Andrews, J. C.; Ice, G. E.; Pianetta, P.; Nanda, J. Nanoscale Morphological and Chemical Changes of High Voltage Lithium-Manganese Rich NMC Composite Cathodes with Cycling. *Nano Lett.* **2014**, *14*, 4334–4341.
- (55) Farmand, M.; Celestre, R.; Denes, P.; Kilcoyne, A. L. D.; Marchesini, S.; Padmore, H.; Tyliczszak, T.; Warwick, T.; Shi, X.; Lee, J.; et al. Near-Edge X-Ray Refraction Fine Structure Microscopy. *Appl. Phys. Lett.* **2017**, *110*, 063101.
- (56) Otsu, N. A Threshold Selection Method from Gray-Level Histograms. *IEEE Trans. Syst. Man Cybern.* **1979**, *1*, 62–66.
- (57) Banterle, N.; Bui, K. H.; Lemke, E. A.; Beck, M. Fourier Ring Correlation as a Resolution Criterion for Super-Resolution Microscopy. *J. Struct. Biol.* **2013**, *183*, 363–367.
- (58) Doube, M.; Klosowski, M. M.; Arganda-Carreras, I.; Cordelières, F. P.; Dougherty, R. P.; Jackson, J. S.; Schmid, B.; Hutchinson, J. R.; Shefelbine, S. J. BoneJ: Free and extensible bone image analysis in ImageJ. *Bone* **2010**, *47*, 1076–1079.
- (59) Poco, J. F.; Satcher, J. H.; Hrubesh, L. W. Synthesis of High Porosity, Monolithic Alumina Aerogels. *J. Non-Cryst. Solids* **2001**, *285*, 57–63.
- (60) Baji, Z.; Lábadi, Z.; Horváth, Z. E.; Molnár, G.; Volk, J.; Bársony, I.; Barna, P. Nucleation and Growth Modes of ALD ZnO. *Crystr. Growth Des.* **2012**, *12*, 5615–5620.
- (61) Hitchcock, A. P.; Toney, M. F. Spectromicroscopy and Coherent Diffraction Imaging: Focus on Energy Materials Applications. *J. Synchrotron Radiat.* **2014**, *21*, 1019–1030.
- (62) Kaznatcheev, K. V.; Karunakaran, C.; Lanke, U. D.; Urquhart, S. G.; Obst, M.; Hitchcock, A. P. Soft X-Ray Spectromicroscopy Beamline at the CLS: Commissioning Results. *Nucl. Instrum. Methods Phys. Res., Sect. A* **2007**, *582*, 96–99.
- (63) Jacobsen; Wirick; Flynn; Zimba. Soft X-Ray Spectroscopy from Image Sequences with Sub-100 Nm Spatial Resolution. *J. Microsc.* **2000**, *197*, 173–184.
- (64) Hitchcock, A. P. aXis2000 Is Written in Interactive Data Language (IDL). It Is Available Free for Non-Commercial Use from <http://unicom.mcmaster.ca/aXis2000.html>. last accessed 10 Oct, 2018.
- (65) Shapiro, D. A.; Celestre, R.; Denes, P.; Farmand, M. Ptychographic Imaging of Nano-Materials at the Advanced Light Source with the Nanosurveyor Instrument. *J. Phys.: Conf. Ser.* **2016**, *849*, 12028.
- (66) Marchesini, S.; Krishnan, H.; Daurer, B. J.; Shapiro, D. A.; Perciano, T.; Sethian, J. A.; Maia, F. R. N. C. SHARP: a distributed GPU-based ptychographic solver. *J. Appl. Crystallogr.* **2016**, *49*, 1245–1252.
- (67) Thevenaz, P.; Ruttimann, U. E.; Unser, M. A Pyramid Approach to Subpixel Registration Based on Intensity. *IEEE Trans. Image Process.* **1998**, *7*, 27–41.
- (68) Wu, J.; Lerotic, M.; Collins, S.; Leary, R.; Saghi, Z.; Midgley, P.; Berejnov, S.; Susac, D.; Stumper, J.; Singh, G.; Hitchcock, A. P. Optimization of Three-Dimensional (3D) Chemical Imaging by Soft X-Ray Spectro-Tomography Using a Compressed Sensing Algorithm. *Microsc. Microanal.* **2017**, *23*, 951–966.
- (69) Beck, A.; Teboulle, M. Fast Gradient-Based Algorithms for Constrained Total Variation Image Denoising and Deblurring Problems. *IEEE Trans. Image Process.* **2009**, *18*, 2419–2434.
- (70) Lerotic, M.; Mak, R.; Wirick, S.; Meirer, F.; Jacobsen, C. MANTiS: a program for the analysis of X-ray spectromicroscopy data. *J. Synchrotron Radiat.* **2014**, *21*, 1206–1212.